Towards Quantitative Evaluation of Tissue Absorption Coefficients Using Light Fluence Correction in Optoacoustic Tomography

Frederic M. Brochu, Joanna Brunker, James Joseph, Michal R. Tomaszewski, Stefan Morscher and Sarah E. Bohndiek

Abstract—**Optoacoustic tomography is a fast developing imaging modality, combining the high contrast available from optical excitation of tissue with the high resolution and penetration depth of ultrasound detection. Light is subject to both absorption and scattering when travelling through tissue; adequate knowledge of tissue optical properties and hence the spatial fluence distribution is required to create an optoacoustic image that is directly proportional to chromophore concentrations at all depths. Using data from a commercial multispectral optoacoustic tomography (MSOT) system, we implemented an iterative optimization for fluence correction based on a finite-element implementation of the delta-Eddington approximation to the Radiative Transfer Equation (RTE). We demonstrate a linear relationship between the image intensity and absorption coefficients across multiple wavelengths and depths in phantoms. We also demonstrate improved feature visibility and spectral recovery at depth in phantoms and with *in vivo* measurements, suggesting our approach could in the future enable quantitative extraction of tissue absorption coefficients in biological tissue.**

Index Terms—**Optoacoustic tomography, molecular imaging, spectral unmixing, light transport.**

I. INTRODUCTION

OPTOACOUSTIC tomography is an emerging imaging modality that uses nanosecond laser pulses to probe the distribution of absorbing molecules, or chromophores, inside soft tissues [1]. Upon absorption, these short energy pulses generate ultrasound waves through the photoacoustic effect; ultrasound transducers can then be used to form an image arising from optical contrast but with higher spatial resolution and penetration depth than is typically permitted with diffuse optical imaging. Measuring tissue response as a function of wavelength enables spectral resolution of different tissue chromophores, such as oxy- and deoxy-hemoglobin.

The optoacoustic image intensity is proportional to the initial acoustic pressure wave generated within a given pixel, which is in turn proportional to the laser light fluence reaching that pixel and the concentration of chromophores within it. The latter is the quantity we ultimately want to measure, by deriving the optical absorption coefficient in the pixel [2]. To achieve such 'quantitative optoacoustic imaging', we require

F M Brochu, J Brunker, J Joseph, M R Tomaszewski and S E Bohndiek are with the Department of Physics and Cancer Research UK Cambridge Institute, University of Cambridge, UK. Corresponding author: S E Bohndiek, e-mail seb53@cam.ac.uk or see http://www.bohndieklab.org.

S Morscher is with iThera Medical GmbH and Institute for Biological and Medical Imaging, Germany.

solutions to both a relatively well studied acoustic inverse problem (e.g. [3]–[6]) as well as a rather more challenging optical inverse problem (e.g. [7]–[14]).

Assuming a well established acoustic image reconstruction methodology, quantification efforts focus on retrieving the light fluence distribution, which is unknown and depends on the distribution of both absorption and scattering coefficients within the sample. Associated challenges include 'spectral coloring' and 'absorption-scattering non-uniqueness'. 'Spectral coloring' refers to modification of the spectrum reaching a given pixel compared to the spectrum incident at the surface, due to wavelength-dependent absorption in overlying tissue [15]. This can lead qualitatively to artifacts in the images and quantitatively to incorrect estimations of chromophore concentrations in deeper tissues. 'Absorption-scattering non-uniqueness' means that in general we cannot recover absorption and scattering distributions simultaneously and uniquely from a single measurement of the absorbed energy density, since both factors can directly affect the fluence distribution. It therefore not possible to say whether deviations between the measured and calculated energy density are due to an error in the absorption coefficient (μ_a) or scattering coefficient (μ'_s) [11]. While the latter challenge can be mitigated with multiple light sources or wavelengths [11], [16] (as used here), the former remains a significant problem for quantitative optoacoustic imaging *in vivo*.

In order to compensate for spectral coloring and extract quantitative chromophore concentrations, we must have knowledge of the light propagation through the entire object. While non-invasive, non-destructive assessment of the light field in tissues *in vivo* is possible in principle [17]–[19], in practice it usually requires complex (and often expensive) additional instrumentation, hence the light fluence distribution is frequently modeled. Fortunately, there are a number of mathematical and numerical models that can be used to describe light propagation in optically absorbing and scattering media, reviewed comprehensively in [20]. Naturally, the speed of computation must be traded against the accuracy of the derived light fluence map. Using the random walk approach of Monte Carlo methods is considered the gold standard, but the computation time required is often significant making it unsuitable for iterative approaches, which calculate the fluence multiple times [20]. The Radiative Transfer Equation (RTE) is commonly used, which expresses the conservation of energy during the absorption and scattering processes, characterizing

tissue by μ_a, μ'_s, and a 'phase function' that describes the directionality of the scattering process [11]. Approximations can be made in highly scattering media to obtain simpler solutions. The diffusion approximation is applicable when the directional dependence of the light fluence is weak; a limitation is that it cannot be used close to the tissue surface (within $1/\mu'_s$). The δ-Eddington approximation overcomes this limitation [21] resulting in a separation of the fluence into collimated and scattered components, which maintains an accurate description in the surface region and at depth. This property makes it highly relevant for application in tissue. The δ-Eddington approximation to the RTE has been shown to provide similar results to Monte Carlo but with a much faster computation time [22].

To establish methodology for quantitative optoacoustic imaging that can be applied robustly *in vivo*, we chose to use an established acoustic reconstruction methodology [23] and the δ-Eddington approximation to the RTE. Under the condition of constant Grüneisen parameter and well modelled light fluence, there should exist a linear relationship between the initial pressure amplitude measured in the optoacoustic image and the absorption coefficient. We hypothesized that the use of a light fluence model to correct our image data would overcome spectral coloring and enable the linear relationship, which is not present in our raw data, to be recovered. To implement the correction, we used a finite-element method [7]. Importantly, we segmented the optoacoustic images into a small number of regions with distinct optical properties, which form the base of the iterative optimization loop [24] and speed up the convergence. We found that this implementation not only provided the expected linear relationship between the optoacoustic pixel intensities and the known absorption coefficient in tissue mimicking phantoms, but was also able to compensate for spectral coloring. Translating the correction procedure to *in vivo* data, we saw an improvement in the visualization of structures at depth (> 5mm) within the mouse.

II. MATERIALS AND METHODS

A. Light fluence model and correction algorithm

Optoacoustic images are formed by reconstructing the original point source of the acoustic waves generated by the absorption of the laser pulse, as measured by ultrasound transducers placed around the object. The pixel intensity $V(\underline{r})$ in these images is usually expressed as a function of the voltage readings from the transducers and is related to the absorption coefficient distribution $\mu_a(\underline{r})$ through the system response α and the thermo-elastic Grüneisen parameter Γ (both assumed spatially invariant), the reduced scattering coefficient $\mu'_s(\underline{r})$ and the light fluence Φ within a resolution limited elementary volume at position $\underline{r}$ as shown in Equation 1:

$$V(\underline{r}) = \alpha\Gamma\mu_a(\underline{r})\Phi[\underline{r}, \mu_a(\underline{r}), \mu'_s(\underline{r})] \qquad (1)$$

Calculating the distribution of laser light over the entire imaged object is not trivial, because the fluence distribution Φ and the pixel intensity $V(\underline{r})$ in Equation 1 both depend on $\mu_a(\underline{r})$. To overcome this difficulty, we implemented an iterative optimization based on the modeling of the light
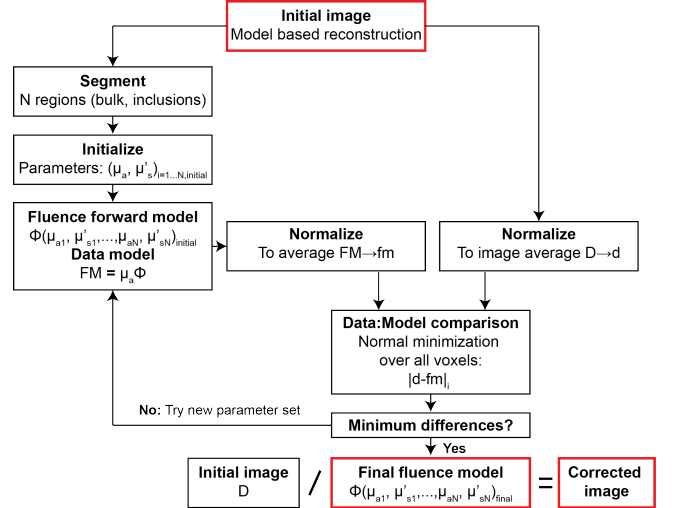

Figure 1: Schematic of the optimization procedure used to extract the light fluence distribution and perform fluence correction.

fluence from the distributions of absorption and scattering coefficients in the imaged object. The optimization algorithm is illustrated in Figure 1.

The optimization procedure commences from the initial image, which is reconstructed in 2D using a model-based acoustic reconstruction (see below) [23]. To improve the speed of convergence of the optimization, we then use *a priori* knowledge of the structure of the object from the initial image to segment the object into regions, within which $\mu_a(\underline{r})$ and $\mu'_s(\underline{r})$ are assumed to be constant. Each region is allocated a set of expected optical properties [$\mu_a(\underline{r})$ and $\mu'_s(\underline{r})$] during the initialization that will be tuned during the optimization procedure. While this is clearly a valid assumption within simple phantoms, it could break down within more complex systems such as living subjects, which have a wide distribution of expected absorption and scattering values [25]. As we are operating in the near-infrared window, where absorption by hemoglobin dominates other chromophores by over two orders of magnitude, the spectral profile of a given organ will be dominated by how blood rich and perfused it is. Variations in hemoglobin concentration and oxygenation within a given organ are small (less than 20%, even in the kidney where the medulla is hypoxic relative to the cortex), compared to the variation between organs (which can be of order of magnitude). We therefore decided to segment our *in vivo* slice data at the organ level rather than to account for intra-organ heterogeneity in this initial study. Further experimental work would be needed to establish the heterogeneity of optical absorption and scattering within organs such as the kidney and spleen, since published values are normally given on a per-organ basis [25], [26].

The light fluence model used in the optimization is a δ-Eddington approximation to the Radiative Transfer Equation [8], [22], [27], shown to perform well at the surface and deep inside an imaged object [22], [27]. It was implemented using a finite-element approach [28] on a GPU card to

speed up the computation time [29]. The optimization procedure was implemented in MATLAB (Mathworks), using the minimization function 'fmincon()' with no cap on the maximum number of allowed iterations. Convergence was typically reached within 150 iterations for 5 regions of interest. We also implemented patternsearch, ga and simanneal (all available within the MATLAB Global Optimization Toolbox) for comparison, but these failed closure tests based on data prepared using a forward model with defined $\mu_a(\underline{r})$ and $\mu'_s(\underline{r})$. The absorption coefficients were left free to vary over a wide range between 0 and 10 cm^{-1}, while the scattering coefficients were tightly constrained to vary within 10 % (using hard bounds 0.9 to 1.1) of their nominal values for phantoms [30] and mouse organs [26]. Relaxing the constraint on $\mu'_s(\underline{r})$ (to hard bounds in the range 0.1 to 5) revealed greater variation in the extracted fluence maps, especially for the *in vivo* data, but repeated application of the narrow constraint (0.9 - 1.1) reliably produced the same $\mu_a(\underline{r})$ and $\mu'_s(\underline{r})$ pair.

We performed the computation on 2D slices using a 2D fluence model, which has been shown to be an accurate approximation to a 3D model in the case of phantoms with uniform optical properties in the out-of-plane (z) direction [13]. Although we found that in phantoms, the 2D model performed better than the equivalent model in 3D with 21 illuminated slices (which required all available memory to store the MATLAB matrix), we anticipate that the 2D model may not be generalizable to all complex cases encountered *in vivo*. To perform these initial studies *in vivo*, we therefore chose a central slice within an organ, so that the optical properties would be relatively smoothly varying and symmetric out-of-plane (see Section II-D). For a typical slice (332x332 pixels), 2D modeling takes on average 2.5 min for 10 optimization variables (5 regions) on AMD Radeon R9 200 series with 4 Gb memory and 1250 MHz memory clock.

The minimization function is the pixel-by-pixel norm of the difference between modeled and raw intensities from the initial image. Both the modeled and raw data are normalized to their integrals, as the global scale factor between the raw data and the model is not known. Due to this normalization we do not at present use the optical parameters $(\mu_a(\underline{r}), \mu'_s(\underline{r}))$ returned by the fit. Instead, the pattern of the light fluence across the object is used to correct the initial image, the result of which is then used for spectral analysis (see Section II-C). The fluence correction is applied by dividing pixel-by-pixel the initial image with the final fluence model (Figure 1). The fluence correction algorithm is run independently for each different wavelength and imaged slice.

From Equation 1, one can derive the relationship between the image intensity V(r) and the absorption parameter $\mu_a(\underline{r})$. If we make the assumption that the Grüneisen parameter Γ has no spatial dependence within the object, then the only parameter with unknown spatial dependence in Equation 1 is the fluence. Hence, provided that we derive the spatial component of the fluence correctly, we expect to achieve a linear relationship between V(r) and $\mu_a(\underline{r})$ across the entire image.
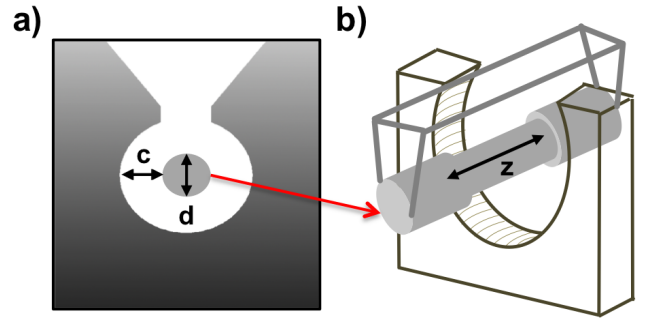

Figure 2: The geometry of the MultiSpectral Optoacoustic Tomography (MSOT) system used in the study. (a) Phantoms (of diameter d = 2cm) or mice are suspended a distance c = 3 cm from the cylindrical array of focused transducers using a custom holder as shown in (b). The holder can be translated in the z direction through the detection plane.

B. MultiSpectral Optoacoustic Tomography system

Imaging was performed with a commercial small animal MultiSpectral Optoacoustic Tomography (MSOT) system (iThera Medical), the geometry of which is shown in Figure 2. The system has been described in detail elsewhere [31]. The sample is suspended from a custom holder that aligns it with the center of the transducer ring and immersed in heated water for ultrasound coupling via a polyethylene membrane. 3D tomography is achieved by moving the sample through the transducer ring. A tunable (660 - 1200 nm) pulsed laser with pulse width <10 ns and repetition rate of 10 Hz excites the sample through a multi-arm fiber bundle, which provides a homogeneous, 360-degree illumination over a cylindrical geometry. The resulting acoustic waves are simultaneously detected by a ring of ultrasound transducers arranged over an azimuthal span of 270-degrees around the cylinder (Figure 2) whose frequency response is best characterized by a Gaussian with peak sensitivity at 5 MHz and a transmit/receive bandwidth of 60%. This detection geometry allows for resolution of approximately 150μm in the imaging plane and 900μm out of plane. The reconstruction algorithm includes an electrical impulse response correction, which accounts for the Gaussian response of the ultrasound transducers by deconvolving a reference impulse response from the measured acoustic signals. The reference impulse response is based on the vendor specifications for transducer performance, the key parameters of which (5 MHz center frequency, 60% bandwidth) were verified by the manufacturer of the supplied transducer array using pulse-echo ultrasound. The transducer time series signals are then reconstructed into 2D pressure maps using the default settings supplied with ViewMSOT v3.6 and the linear model-based reconstruction algorithm [23] with a pixel size of 100 μm. The algorithm calculates an accurate forward model of the detection geometry and inverts it to determine the acoustic source distribution that is the base for the aforementioned correction algorithm. Negative pixel values are set to zero and ignored in the analysis since they have no physical meaning in the sense of generated pressure or absorption; they reflect

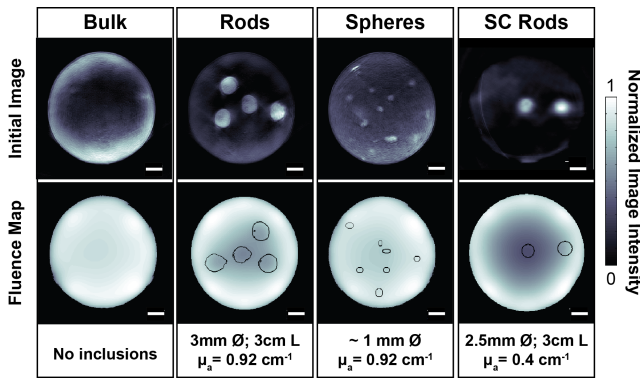| Bulk	Rods	Spheres	SC Rods
No inclusions	3mm Ø; 3cm L μ_a= 0.92 cm^{-1}	~ 1 mm Ø μ_a= 0.92 cm^{-1}	2.5mm Ø; 3cm L μ_a= 0.4 cm^{-1}

Figure 3: Examples of initial images (upper) and fluence models (lower) from the phantoms used in this study. Inclusion boundaries are shown as black contours on the fluence models. The absorption coefficients given in the bottom row refer to the dye present in the phantom inclusions. Phantoms were produced containing: 1) only bulk; 2) rod inclusions at 4 positions; 3) sphere inclusions; or 4) rod inclusions at 2 positions for spectral coloring (SC) studies. In cases 1-3, bulk (μ_a = 0.06 cm^{-1}) and inclusions (μ_a as stated) were fabricated in duplicate using a. Indian Ink or b. nigrosin dye. For case 4, bulk contained indocyanine green (μ_a = 0.15 cm^{-1}) while the inclusions contained nigrosin (μ_a = 0.4 cm^{-1}). All phantoms contain intralipid to define the scattering as μ_s'= 5 cm^{-1}. Scale bar = 3 mm; z scale 0 (min) to 1 (max) in all cases.

artifacts resulting from the imperfect system geometry. The resulting image is the 'initial image' in Figure 1.

C. Phantom data acquisition and analysis

For clarity, the four different phantom types used in this paper are summarized in Figure 3. All materials were purchased from Sigma Aldrich unless otherwise stated. Phantoms containing a range of optical properties in the bulk and inclusions were used to establish and validate our model. Gels were used to produce phantoms with 20 mm radius by mixing 1.5 % w/v agar with: 1) a known absorber to define the absorption properties of the phantom; and 2) intralipid to define the scattering as μ_s'= 5 cm^{-1} at a reference wavelength of 800 nm [32].

The first phantom set for calibration, with rod and sphere inclusions and varying bulk absorption, was used to test the expected linear relationship between absorption coefficient and optoacoustic image signals. Rods were defined using 3D printed molds placed within the bulk, which were removed after the bulk had set to allow the introduction of liquid agarose with different absorption properties. Absorption values were defined using the relatively flat absorber Indian Ink (Higgins) and verified at wavelengths between 700 and 900 nm in 50 nm steps using a plate reader (Molecular Devices), before the incorporation of agarose powder. The inclusion absorber concentration is 0.92 cm^{-1} at a reference wavelength of 800 nm. Multiples of this concentration (0, 1/16, 1/8, 1/4 and 1/2) were used for the bulk, generating a phantom set with

constant inclusion and varying bulk absorptions. Negligible changes to the measured quantities were observed in response to incorporation of agarose powder. Phantoms with "0 cm^{-1}" have no indian ink and the residual absorption from all other components (agar, intralipid) is smaller than 0.01 cm^{-1} in the wavelength range of our laser [30]. We repeated all measurements for a phantom of fixed bulk but varying rod absorption coefficients using nigrosin rather than Indian Ink as the absorbing dye, to test the robustness of the approach to different dyes and different imaging systems (see below).

The second phantom set for spectral coloring, with two distinct absorbers at fixed concentrations, was used to test the impact of fluence correction on spectral coloring. Absorption values were defined using indocyanine green (ICG) for the phantom bulk and nigrosin for the inclusions and were verified at wavelengths between 660 and 900 nm in variable steps using a plate reader (BMG Labtech), to ensure adequate coverage of the ICG absorption peak. Final phantom concentrations corresponded to absorption values of 0.15 cm^{-1} for ICG and 0.4 cm^{-1} for nigrosin at a wavelength of 779 nm. We prepared two rod inclusions, each with a diameter of 3 mm, one at the center of the phantom and one near the surface to compare the impact of spectral coloring as a function of depth.

MSOT for both sets of phantoms was performed using 20 frame averages. The chromophore concentrations can be established using spectral analysis [15], based on the linear relationship between the measured pixel intensity and the absorption coefficients of the identified chromophores μ_a^i:

$$\mu_a(\lambda) = \sum_i \mu_a^i(\lambda) = \sum_i c_i \epsilon_i(\lambda) \quad (2)$$

where c_i is the concentration of an identified chromophore species i and $\epsilon_i(\lambda)$ is the associated molar extinction coefficient. Extinction curves for Equation 2 were obtained from the verification measurements of phantom absorbers, allowing extraction of the chromophore concentrations through simple linear inversion, referred to as 'unmixing'. The linear unmixing was applied to both initial and fluence corrected images from the spectral coloring phantoms and the accuracy of the fit (as assessed by the χ^2 parameter) was used to quantify the impact of fluence correction.

Qualitatively, the fluence models (Figure 3) show that small spherical inclusions have little influence on the fluence distribution (compared to the bulk phantom), however, large cylindrical inclusions (rods) reduce the amount of light available in the center. All phantom data were acquired at a fixed water bath temperature of 34 degrees Celsius. The first phantom set containing rods and spheres used in this paper was imaged using a 128-element transducer (inVision 128), while the remaining data was acquired using an upgraded model featuring 256 detector elements (inVision 256). We verified by repeating the rod phantom experiment in both versions of the system that the change in transducer number did not impact the studies performed here since the acoustic properties remained the same. Constant values of the absorption coefficient were taken within each region defined by the segmentation, hence by construction, the distribution is step-wise constant; to take into account possible phantom imperfections (e.g. drift of the

rod axis), we use image segmentation data rather than the ideal blueprint phantom geometry for our computations of light fluence. This segmentation is performed manually in MATLAB. Each inclusion is treated as an independent region in the optimization, even though inclusions are all made from the same mixture. Error bars shown are standard error of the mean throughout the paper.

D. In vivo data acquisition and analysis

All animal procedures were conducted in accordance with project and personal licenses issued under the United Kingdom Animals (Scientific Procedures) Act, 1986. Healthy nude mice (Charles River; n = 4) were anesthetized with 1.5-2% isoflurane for the duration of the imaging and maintained at 36 degrees Celsius. Mice were allowed to stabilize within the system for approximately 15 minutes prior to imaging and respiration was maintained at a constant rate by changing the level of isoflurane as required. Nude mice do not possess skin melanin, so for this study the dominant chromophores were oxy- and deoxy-hemoglobin, which at physiologically relevant concentrations have absorption coefficients two orders of magnitude greater than water and fat. In order to explore the impact of systemic oxygenation on the performance of our light fluence correction, we mixed the isoflurane anesthetic with either medical air or 100 % oxygen. An imaging slice was recorded from the torso of the mice centered on the kidneys and spleen. MSOT was performed between excitation wavelengths of 690 and 880 nm in 10 nm increments, with 10 frame averages. For *in vivo* data, image segmentation was performed manually by delineating the major organs present in the slice. Contouring individual small blood vessels is not possible with the limited resolution of the imaging data; only larger vessels such as the aorta and inferior vena cava are considered separately.

Scattering coefficients for mouse tissues from [26] are used to initialize the fluence model, applying muscle values for the spine region, blood for the larger, resolvable, blood vessels and adipose for unspecified regions ("bulk"). For biological data, the μ_s' bounds of 0.9-1.1 are likely a conservative estimate given physiological and trans-species variations. After application of the model, fluence correction was first applied to data from each individual wavelength, then oxy- and deoxy-hemoglobin concentrations were extracted from image data using the simple linear regression from Equation 2. Reference spectra were derived from the literature [33]. All spectral data shown are normalized to the pixel with highest fluence in the map at 690 nm to enable comparison across data sets. For the comparison of gas breathing, we define oxygen saturation, SO_2^{MSOT}, as the ratio of our extracted oxy- and total hemoglobin (oxy- plus deoxy-hemoglobin) weighted signals from the linear regression data.

III. RESULTS

A. Phantom data

Calibration phantoms: Figure 4 provides a graphical illustration of a single slice optimization. The algorithm starts from the segmented image (Figure 4 (a)) using an arbitrary starting
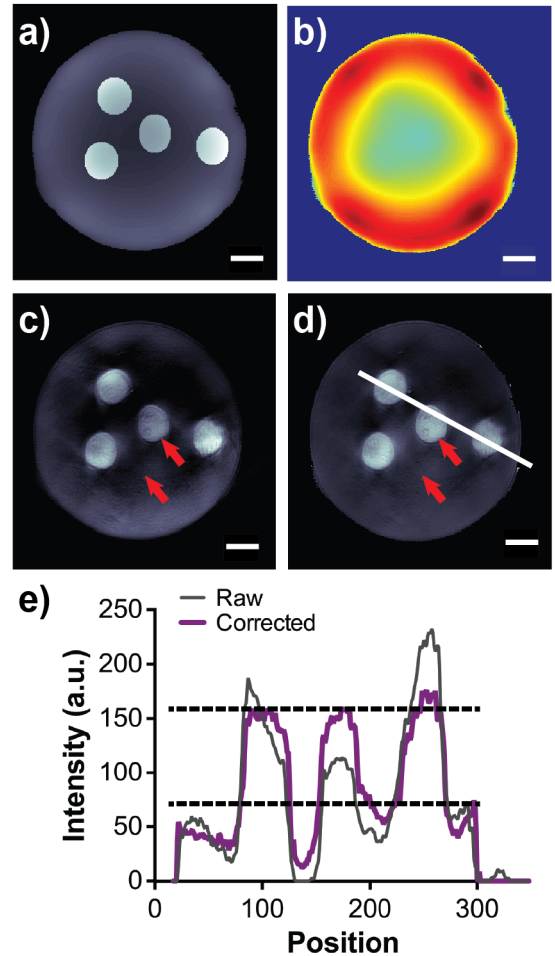

Figure 4: Illustration of the algorithm application in a single slice of a phantom with rod inclusions μ_a= 0.92 cm^{-1} and bulk μ_a= 0.23 cm^{-1}. (a) Model of image from best fitting light fluence parameters. (b) Fluence distribution resulting from the optimization procedure. (c) Initial image. (d) Image after fluence correction. (e) Data extracted from the line profile intersecting multiple rods, illustrated in (d). Red arrows indicate artificially low image intensity in (c) due to optical attenuation that are corrected in (d). Scale bar = 3 mm

point value for the absorption coefficient and iteratively generates fluence maps (Figure 4 (b)) based on the segmentation, varying the optical parameters of each defined region from the segmented image until the modeled image resembles the initial image (Figure 4 c). The fluence model (Figure 4 (b)) and fluence corrected image (Figure 4 d) are both output from the algorithm. It can be observed qualitatively that before correction (Figure 4 c, red arrows), the intensity of the inner rod appears lower than the outer rods, despite having the same absorption coefficient. In addition, the inner regions of the bulk appear darker compared to the outer regions. These artifacts due to optical attenuation in overlying media are removed upon fluence correction (Figure 4 (d)). To visualize this quantitatively, a line profile (illustrated on Figure 4 (d)) was drawn through the phantom, covering bulk and inclusions

(Figure 4 (e)). In the raw data, the peaks corresponding to the absorbing inclusions show a strong gradient in their intensity between the outer and inner surfaces of the inclusion, while the bulk signal exhibits a soft, radial decay (akin to beam hardening in X-ray imaging). After correction, the radial decay of the bulk is reduced in magnitude and the fluence-related artifact in the inclusions is almost completely removed.

A linear relationship between the reconstructed pixel intensity V($\underline{r}$) and the measured absorption coefficients for all regions in the first phantom set was not present in the raw data and was only established after fluence correction (Figure 5 (a)). Data in Figure 5 (a) were compiled from all regions (bulk and inclusions) defined by segmentation, across all wavelengths, and with both indian ink- and nigrosin-based phantoms within the first phantom set. These data illustrate the consistency of the fluence correction result across multiple phantoms and absorbers. Data is shown as the average of measurements over multiple slices and different phantoms regions with identical known absorption, hence the error bars are largely contained within the plotted points. The linear relationship is quantitatively reflected in the parameters of the fit (constrained to pass through $x = 0$, $y = 0$), which were more tightly constrained following correction (raw slope: 0.94 ± 0.05, $S_{y.x} = 0.32$; corrected slope: 0.77 ± 0.02, $S_{y.x} = 0.16$). Measurements below 0.7 cm^{-1} are bulk measurements, while those beyond are inclusion measurements. The raw data shows a linear relationship to the measured absorption coefficient only below 0.15 cm^{-1}, while it is maintained up to 2.5 cm^{-1} after fluence correction. This is further illustrated by the residuals of the linear fit, which were far lower for the corrected data and are shown in Figure 5 (b).

Using the fact that the rod phantom contained inclusions at well defined positions near the center and near the surface of the phantom, we calculated intensity ratios between the inner inclusion and the outer ones to quantify the effect of bulk attenuation (Figure 5 (c)). Since all inclusions are made from the same mixture, the intensity ratio between inner and outer inclusions is expected to be 1 if the light propagation to the site of absorption is correctly accounted for. The application of the light fluence correction produces a statistically significant increase in the intensity ratio, from 0.79 ± 0.01 to 0.95 ± 0.01 for bulk $\mu_a = 0$ cm^{-1} and 0.72 ± 0.01 to 0.897 ± 0.005 for bulk $\mu_a = 0.23$ cm^{-1} ($p < 0.0001$ in both cases).

Spectral coloring phantoms: Spectral coloring refers to the impact of the absorption spectrum of more superficial chromophores within a sample on the recorded data at depth. To explore this effect, we used the second phantom set to extract the influence of the peaked absorption spectrum of ICG on the recorded spectrum of the nigrosin dye, which is monotonically decaying within our wavelength range. Intensity spectra of the phantom inclusions can be seen in Figure 6, while fit residuals and intensity ratios calculated between the inner and outer inclusions are in Figure 7.

From Figure 6 (a), it is clear that spectral coloring is impacting the raw data, since a minimum appears in the nigrosin spectra at the peak absorption of the ICG spectrum for both inner and outer inclusions. This trend was removed after fluence correction as shown in Figure 6 (b), although
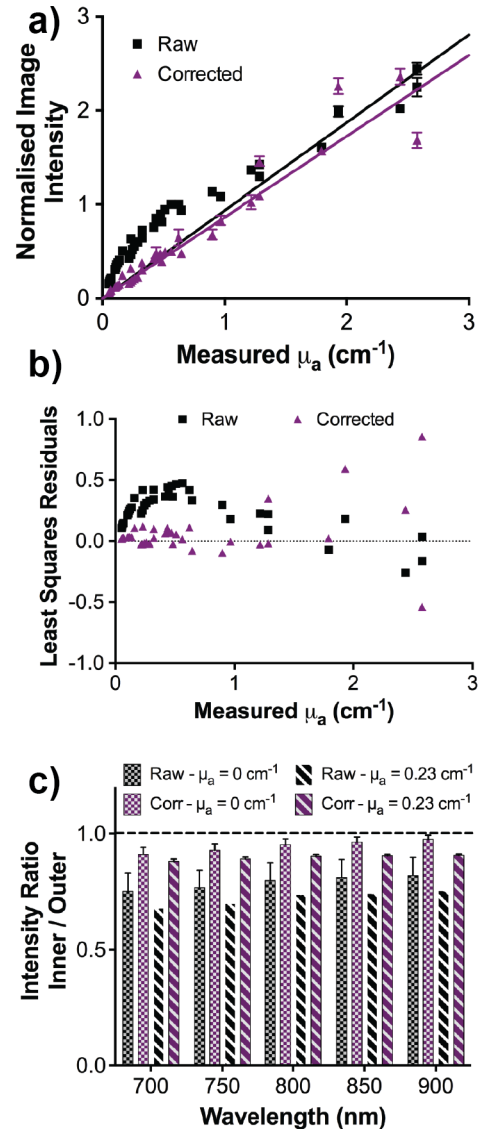

Figure 5: Image intensity as a function of the measured μ_a of the phantom materials is nonlinear in the raw data but is linearized as a result of the fluence correction (a). The residuals of the linear fit (constrained to pass through $x = 0, y = 0$) are lower (b) in the corrected data. (c) The application of the light fluence correction produces a statistically significant increase in the intensity ratio (c), from 0.79 ± 0.01 to 0.95 ± 0.01 for bulk $\mu_a = 0$ cm^{-1} and 0.72 ± 0.01 to 0.897 ± 0.005 for bulk $\mu_a = 0.23$ cm^{-1} ($p < 0.0001$ in both cases).

some 'overcompensation' is seen at the wavelengths closest to the peak absorption (775, 779, 800nm). Nonetheless it is evident from Figure 7 (a) that the absolute difference between the image intensity data and the pure nigrosin spectrum is consistently smaller after correction for all wavelengths. The ratios (Figure 7 (b)) calculated for the raw data vary as a function of wavelength, reproducing the negative of the peak of the ICG, as the bulk absorption is not accounted for at this stage. Despite this, we found an overall improvement in the average ratio, which increased from 0.86 ± 0.02 to 1.03 ± 0.05 following correction ($p = 0.02$).

We were also able to establish the effect of fluence correction on the extracted chromophore concentrations by linear unmixing according to Equation 2. Numerical results are detailed in Table I for linear unmixing performed on raw and fluence corrected data. As expected, in Figure 6 fluence correction has the greatest impact on the inner inclusion, and this is also evident in Table I by the improvements in fit quality, expressed as Pearson's χ^2 test. After correction, there are similar fit qualities for both the inner and outer inclusions and the bulk; in addition, the linear unmixing results for the outer inclusion (nigrosin) and the bulk (ICG) are close to the ground truth (unity). The fluence correction does not produce an improvement in the linear unmixing results for the inner inclusion, and this is likely due to the 'overcompensation' at wavelengths close to the ICG peak absorption.

B. In vivo mouse data

Following validation in phantom data, the fluence correction procedure was then applied to data acquired *in vivo* from nude mice. Figure 8 shows qualitatively the effect of the correction applied at 690 nm, where deoxyhemoglobin absorption dominates, and at 880 nm, where the dominant contribution is from oxyhemoglobin. The segmentation used during the optimization procedure is also shown. As expected from our phantom data, the fluence exhibits a radial decrease from the surface to the center. Less light penetrates to the center of the mouse at 690 nm than at 880 nm, due to the higher degree of absorption and scattering at the shorter wavelength. The asymmetric distribution of the fluence is likely due to the presence of the spleen on one side of the mouse, which is a highly absorbing blood rich organ. Following application of the fluence correction, a clear enhancement of the central features (aorta, vena cava, inner part of the kidney) can be seen compared to the raw image, as made clear in the line profiles of Figure 8. In particular, the aorta, which carries oxygenated blood, is more clearly visible after correction in the 880 nm data as expected due to the spectral dominance of oxyhemoglobin in this region.

To investigate the effect of spectral coloring *in vivo*, we defined two independent regions of interest in the kidney, one in the outer cortex and one in the inner cortex (Figure 9 (a)), as well as regions of interest within the aorta and inferior vena cava (IVC). The normalized intensity spectra before and after fluence correction in each region of interest are shown in Figure 9. All spectral data are normalized as per image data to enable comparison across data sets. From Figure 9, it is clear
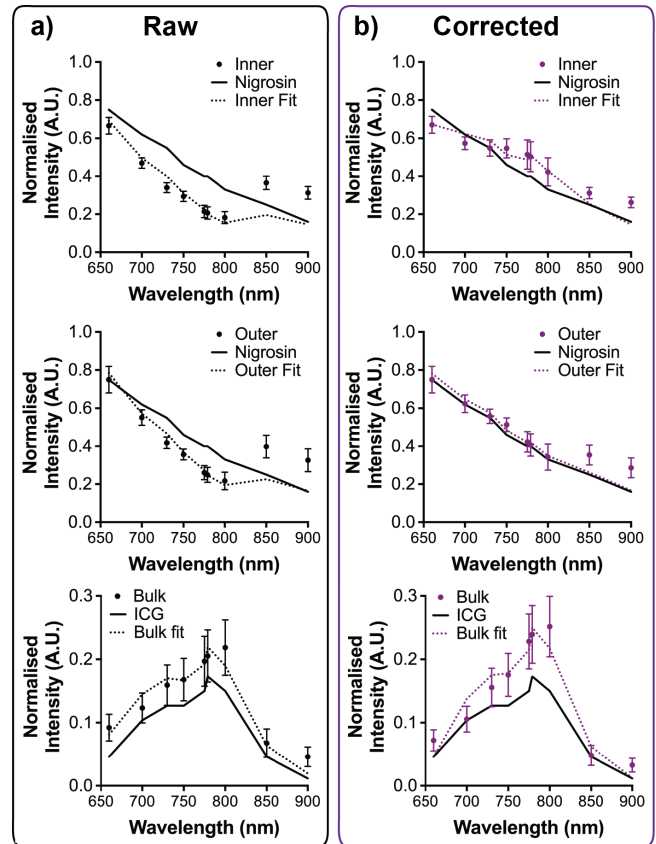

Figure 6: Intensity spectra of inner and outer rod inclusions in the spectral coloring phantom, before (a) and after (b) fluence correction. Overlaid curves are the absorption spectra of the dye (measured independently; solid line) and spectral unmixing results (calculated from data; dashed lines). Qualitatively it is clear that the absorption spectrum of ICG in the bulk impacts the raw nigrosin spectra, but the effect is largely negated after fluence correction. All data are rescaled to the reference point of 660 nm for comparison. Associated least squares residuals and intensity ratios of the rod inclusions are shown in Figure 7.
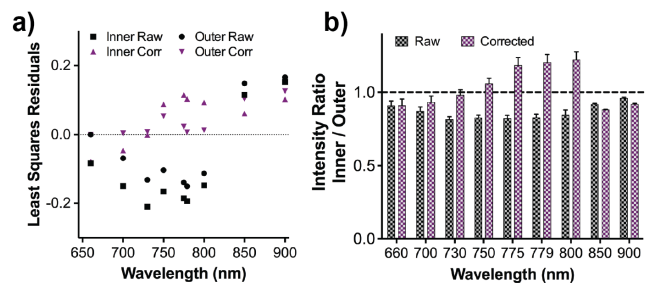

Figure 7: Performance of the spectral coloring compensation in phantoms. (a) The least squares residuals of the data in Figure 6. (b) Intensity ratios between the inner and outer inclusions in the spectral coloring phantom as a function of the imaged wavelength; the average ratio increased significantly from 0.86 ± 0.02 to 1.03 ± 0.05 following correction ($p = 0.02$)

	Fit (optimum=0)		Unmixing (optimum=1)	
	χ^2 fit	χ^2pure	Nigrosin	ICG
Bulk Raw	0.3	0.6	0.116 ± 0.003	0.884 ± 0.004
Bulk Corr	0.5	0.3	-0.086 ± 0.002	0.91 ± 0.03
Inner Raw	0.9	1.7	0.792 ± 0.007	-0.21 ± 0.01
Inner Corr	0.2	0.3	0.784 ± 0.004	0.22 ± 0.08
Outer Raw	0.7	1.2	0.81 ± 0.03	-0.190 ± 0.005
Outer Corr	0.2	0.2	0.99 ± 0.02	0.01 ± 0.04

Table I: Fit quality of raw and fluence corrected (corr) data acquired with the spectral coloring phantom also analysed in Figure 6 and Figure 7. "χ^2 fit" and "χ^2 pure" refer respectively to a fit to the unmixing results and to the relevant pure component (ICG for the bulk and nigrosin for the inner and outer inclusions). For all χ^2 values, the number of degree of freedom is 11. For the linear unmixing results, fractions are defined such that the sum of the absolute values of each component is 1.
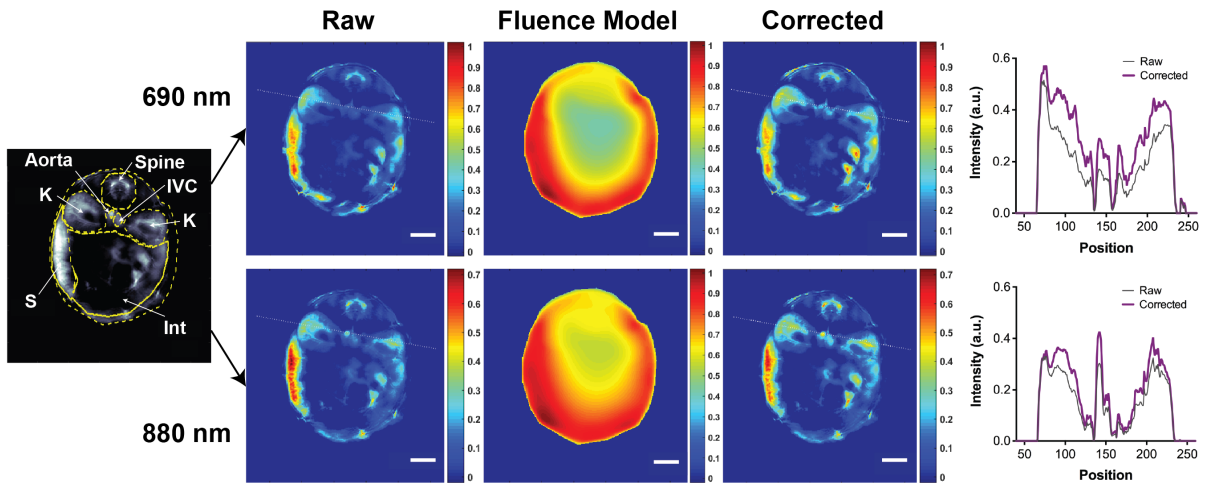

Figure 8: The application of fluence correction *in vivo* to an image slice through several blood rich organs, including the kidneys and spleen. The result of applying the fluence correction is an enhancement of the central image features, including the aorta, inferior vena cava, and the inner part of the kidney. Line profiles are shown to better illustrate the impact of fluence correction. Raw and corrected data are normalized to the pixel with highest fluence in the map at 690 nm for comparison. K = kidney, S = spleen, IVC = inferior vena cava, Int = intestine. Scale bar = 3 mm

that fluence correction mostly affects central features (aorta, IVC and inner kidney cortex), increasing their intensity for all wavelengths as well as changing the spectral shape. While a general enhancement across all wavelengths is seen for the aorta, the fluence compensation tends to differentially enhance the shorter wavelengths for the kidney and IVC regions of interest.

Spectral unmixing of the contributions of oxy- and deoxy-hemoglobin was also performed, using a simple linear inversion with two components: oxy- and deoxyhemoglobin (excluding negative pixels, which were set to 0). Oxygen saturation, SO_2^{MSOT}, was taken as the ratio of the extracted oxy- and total hemoglobin (oxy- plus deoxy-hemoglobin) weighted values from the linear unmixing data. We compared the data acquired when the mice were breathing medical air (21% oxygen) or 100% oxygen. The raw and fluence corrected SO_2^{MSOT} values averaged over the entire region of interest (Figure 9 (a)) and across all four mice are shown in Table II. The relative SO_2^{MSOT} values are consistently lower than the expected physiological SO_2 values, which may be due to the fact that our simple linear unmixing provides only oxy-

and deoxy-hemoglobin weighted images, rather than absolute concentrations. Interestingly, the fluence correction produces no significant change in the extracted SO_2^{MSOT} values.

IV. DISCUSSION

The goal of this study was to accurately recover the spectral profile of excitation light used for optoacoustic tomography. By accurately modeling light fluence in the data reconstruction, we ultimately hope to enable quantitative imaging of deep tissue chromophore concentrations. Here, we took the first steps in implementing the light fluence model for phantom and *in vivo* data.

Our first key finding is that light fluence correction allows us to establish a linear relationship between the reconstructed image intensity and independently measured absorption coefficients up to 2.5 cm^{-1} in agarose gel phantoms. Moreover, the light fluence correction compensates for spectral coloring due to bulk absorption and quantitatively improves the spectral unmixing of chromophores in phantoms as evidenced by the Pearson's χ^2 test. These data indicate that our model provides

	Raw data		After fluence correction	
Organ	Medical Air	100 % Oxygen	Medical Air	100 % Oxygen
Inner kidney	0.41 ± 0.01	0.51 ± 0.04	0.43 ± 0.02	0.51 ± 0.04
Outer kidney	0.49 ± 0.02	0.51 ± 0.01	0.53 ± 0.05	0.53 ± 0.02
Aorta	0.69 ± 0.03	0.75 ± 0.02	0.71 ± 0.02	0.74 ± 0.01
IVC	0.54 ± 0.03	0.54 ± 0.03	0.56 ± 0.05	0.51 ± 0.03

Table II: SO_2^{MSOT} values for different organs identified in the kidney slice (Figure 9 (a)), before and after fluence correction, under either medical air (21 % O_2) or 100 % O_2 breathing gas. The experiment is repeated over the sample of 4 mice; values are the sample average, and the error bar is the standard error on the mean. IVC = inferior vena cava.
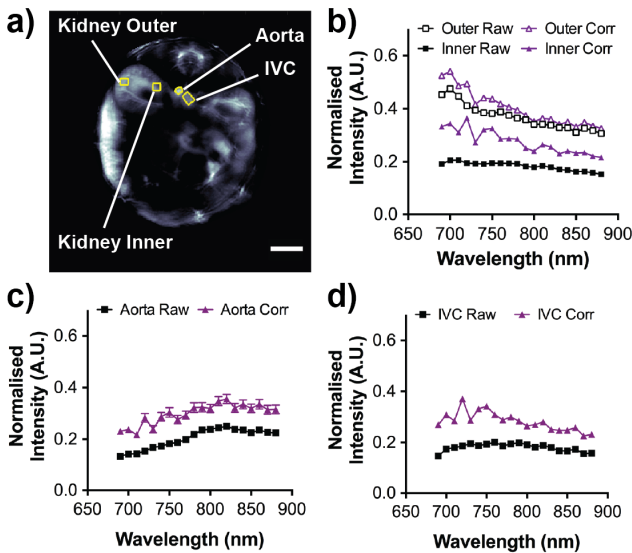

Figure 9: Investigation of *in vivo* spectral coloring in the inner and outer cortex of the kidney, as well as the aorta and inferior vena cava (IVC). (a) Locations of regions of interest used. Intensity spectra are displayed before (squares) and after (triangles) fluence correction for (b) outer and inner kidney cortex, (c) aorta and (d) IVC. The raw and corrected data are normalized to the pixel of highest fluence in the corresponding image at 690 nm. Scale bar = 3 mm.

an accurate compensation for the spatial distribution of light fluence in phantoms under well controlled conditions.

Our second key finding is that our implementation of the light fluence correction algorithm can also be applied to *in vivo* data. Our model depends on the approximate knowledge of the spatial distribution of the optical parameters, which is well controlled for phantoms, but less well known in living tissues. In the latter case, boundaries between regions of distinct optical properties can be blurred and average optical properties depend on the measurement scale, hence it was not obvious that the same approach would be possible. Nevertheless, we chose to manually segment the organs of interest and assign them published values of μ_s' for initialization of the model. Encouragingly, our results show that the application of the correction does improve our ability to visualize organs at depth (> 5 mm into the tissue). It also impacts the observed spectral coloring within the kidney cortex, aorta and inferior vena cava. When these data were combined to perform linear unmixing

to derive oxygenation (SO_2^{MSOT}), however, very little change was observed. Considering the spectra derived within the kidney, fluence correction appears to amplify slightly more the shorter wavelengths, where the deoxyhemoglobin dominates the absorption. However, since blood is predominantly oxygenated, this could explain the negligible change in SO_2^{MSOT} after correction.

There are some limitations to our study. At present, we extract only the geometrical distribution of the fluence function rather than absolute values of absorption coefficient, given our normalization of both the modeled and raw data. We tightly constrained one of our unknowns, the scattering coefficient, to within 10 % of the nominal value in a bid to improve the convergence of our algorithm. Nevertheless, it will be necessary to reduce the number of free parameters to better constrain the problem in future to enable the extraction of absolute absorption coefficients.

The computation of light fluence in 2D potentially places a further limitation for the *in vivo* case. The 2D model has been shown to be an accurate approximation to the 3D model in the case of phantoms, where optical properties in the out-of-plane (z) direction are uniform [13]. For more complex geometries, the validity of this finding is unlikely to generalize. We chose a specific imaging slice *in vivo* through the center of the kidneys and spleen, where we expect the optical properties to be relatively smoothly varying and symmetric out-of-plane. In general, it is likely that absorbers such as blood vessels, adjacent to the imaging plane, will impact the modeled fluence in the slice of interest. Future work will require the use of 3D modeling to investigate the impact of slice-to-slice variation in optical properties on the results from our 2D model and establish the limits within which it can be applied *in vivo*.

We have also assumed a spatially invariant system response α and Grüneisen parameter in order to establish the linear relationship tested in the phantom experiments. Thermal and mechanical properties were maintained in phantoms by using the same material (agar) to form both the bulk and inclusions and we performed measurements at a fixed temperature. In the mouse, however, the Grüneisen parameter may not necessarily be uniformly distributed, although we expect oxy- and deoxy-hemoglobin to share the same Grüneisen parameter, owing to their physical location inside red blood cells [34]. In order to convert our fluence corrected images into quantitative maps of absorption coefficient in appropriate units, we need to independently measure the system response α. We should then confirm the spatial independence of the Grüneisen coefficient

at 36 degrees Celsius *in vivo*. With this information in hand, we could re-build the algorithm to perform optimization without normalization and directly derive the absorption coefficient from Equation 1.

To extend this model robustly for use in biological applications of MSOT, further work is needed to understand the quantitative impact of the correction on the evaluation of hemoglobin concentration and oxygenation, as well as in relation to injected contrast agents. Implementation of an automatic segmentation algorithm would likely be necessary if the algorithm were to be extended to routine use. Ultrasound scans performed independently or within a dual optoacoustic/ultrasound imaging device could help with segmentation. This would have to be coupled with a detailed database of optical properties for mouse tissues to be used by the algorithm as reference values. This approach could speed up the convergence of the fluence model by taking a starting point close to the expected result, with the ultimate aim to perform real-time fluence corrections.

V. Conclusions

We successfully used a finite-element method to evaluate accurately the spatial distribution of light fluence during optoacoustic tomography in phantoms and *in vivo*. Applying the fluence correction resulted in: a direct linear relationship between the reconstructed optoacoustic pixel intensities and the known absorption coefficient in phantoms; improved visualization of structures at depth *in vivo*; and compensation for spectral coloring observed both in phantoms and *in vivo*. These findings pave the way towards quantitative extraction of tissue absorption coefficients and accurate blood oxygenation measurements in the future.

Acknowledgment

References

[1] L. V. Wang and S. Hu, "Photoacoustic Tomography: In Vivo Imaging from Organelles to Organs," *Science*, vol. 335, no. 6075, pp. 1458–1462, 2012.

[2] Y. Wang and R. Wang, "Photoacoustic recovery of an absolute optical absorption coefficient with an exact solution of a wave equation." *Phys. Med. Biol.*, vol. 53, no. 21, pp. 6167–77, 2008.

[3] K. Koestli, M. Frenz, H. Bebie, and H. Weber, "Temporal backward projection of optoacoustic pressure transients using Fourier transform methods," *Phys. Med. Biol.*, vol. 46, pp. 1863–1872, 2001.

[4] G. Paltauf, J. A. Viator, S. A. Prahl, and S. L. Jacques, "Iterative reconstruction algorithm for optoacoustic imaging." *J. Acoust. Soc. Amer.*, vol. 112, no. 4, pp. 1536–1544, 2002.

[5] X. Wang, Y. Xu, M. Xu, S. Yokoo, E. S. Fry, and L. V. Wang, "Photoacoustic tomography of biological tissues with high cross-section resolution: reconstruction and experiment." *Med. Phys.*, vol. 29, no. 12, pp. 2799–2805, 2002.

[6] M. Xu and L. V. Wang, "Universal back-projection algorithm for photoacoustic computed tomography," *Phys. Rev. E - Statistical, Nonlinear, and Soft Matter Physics*, vol. 71, no. 1, pp. 1–7, 2005.

[7] B. T. Cox, S. R. Arridge, K. P. Köstli, and P. C. Beard, "Two-Dimensional quantitative photoacoustic image reconstruction of absorption distributions in scattering media by use of a simple iterative method," *App. Opt.*, vol. 45, no. 8, pp. 1866–1875, 2006.

[8] W. Cong, H. Shen, A. Cong, Y. Wang, and G. Wang, "Modeling photon propagation in biological tissues using a generalized Delta-Eddington phase function," *Phys. Rev. E - Statistical, Nonlinear, and Soft Matter Physics*, vol. 76, no. 5, pp. 1–5, 2007.

[9] B. Banerjee, S. Bagchi, R. M. Vasu, and D. Roy, "Quantitative photoacoustic tomography from boundary pressure measurements: noniterative recovery of optical absorption coefficient from the reconstructed absorbed energy map." *J. Opt. Soc. Am. A*, vol. 25, no. 9, pp. 2347–56, 2008.

[10] L. Yao, Y. Sun, and H. Jiang, "Quantitative photoacoustic tomography based on the radiative transfer equation." *Opt. Lett.*, vol. 34, no. 12, pp. 1765–1767, 2009.

[11] B. T. Cox, S. R. Arridge, and P. C. Beard, "Estimating chromophore distributions from multiwavelength photoacoustic images," *J. Opt. Soc. Am. A*, vol. 26, no. 2, pp. 443–455, 2009.

[12] Z. Yuan and H. Jiang, "Simultaneous recovery of tissue physiological and acoustic properties and the criteria for wavelength selection in multispectral photoacoustic tomography." *Opt. Lett.*, vol. 34, no. 11, pp. 1714–1716, 2009.

[13] J. Laufer, B. Cox, E. Zhang, and P. Beard, "Quantitative determination of chromophore concentrations from 2D photoacoustic images using a nonlinear model-based inversion scheme." *App. Opt.*, vol. 49, no. 8, pp. 1219–33, 2010.

[14] T. Tarvainen, B. T. Cox, J. P. Kaipio, and S. R. Arridge, "Reconstructing absorption and scattering distributions in quantitative photoacoustic tomography," *Inverse Problems*, vol. 28, no. 8, p. 084009, 2012.

[15] S. Tzoumas, N. Deliolanis, S. Morscher, and V. Ntziachristos, "Unmixing molecular agents from absorbing tissue in multispectral optoacoustic tomography," *IEEE Trans. Med. Imaging*, vol. 33, no. 1, pp. 48–60, 2014.

[16] P. Shao, T. J. Harrison, and R. J. Zemp, "Consecutively reconstructing absorption and scattering distributions in turbid media with multiple-illumination photoacoustic tomography," *J. Biomed. Opt.*, vol. 19, no. 12, p. 126009, 2014.

[17] A. Q. Bauer, R. E. Nothdurft, T. N. Erpelding, L. V. Wang, and J. P. Culver, "Quantitative photoacoustic imaging: correcting for heterogeneous light fluence distributions using diffuse optical tomography," *J. Biomed. Opt.*, vol. 16, no. 9, p. 096016, 2011.

[18] L. Yin, Q. Wang, Q. Zhang, and H. Jiang, "Tomographic imaging of absolute optical absorption coefficient in turbid media using combined photoacoustic and diffusing light measurements." *Opt. Lett.*, vol. 32, no. 17, pp. 2556–2558, 2007.

[19] A. Hussain, W. Petersen, J. Staley, E. Hondebrink, and W. Steenbergen, "Quantitative blood oxygen saturation imaging using combined photoacoustics and acousto-optics," *Opt. Lett.*, vol. 41, no. 8, pp. 1720–1723, apr 2016.

[20] B. Cox, J. G. Laufer, S. R. Arridge, and P. C. Beard, "Quantitative spectroscopic photoacoustic imaging: a review." *J. Biomed. Opt.*, vol. 17, no. 6, p. 061202, 2012.

[21] J. H. Joseph, W. J. Wiscombe, and J. a. Weinman, "The delta-Eddington approximation for radiative flux transfer," *J. Atmospheric Sciences*, vol. 33, p. 2452, 1976.

[22] J. Laufer, C. Elwell, D. Delpy, and P. Beard, "In vitro measurements of absolute blood oxygen saturation using pulsed near-infrared photoacoustic spectroscopy: accuracy and resolution." *Phys. Med. Biol.*, vol. 50, no. 18, pp. 4409–4428, 2005.

[23] A. Rosenthal, D. Razansky, and V. Ntziachristos, "Fast semi-analytical model-based acoustic inversion for quantitative optoacoustic tomography," *IEEE Trans. Med. Imaging*, vol. 29, no. 6, pp. 1275–1285, 2010.

[24] T. Jetzfellner, D. Razansky, A. Rosenthal, R. Schulz, K. H. Englmeier, and V. Ntziachristos, "Performance of iterative optoacoustic tomography with experimental data," *App. Phys. Lett.*, vol. 95, no. 1, pp. 2013–2016, 2009.

[25] S. L. Jacques, "Optical properties of biological tissues: a review," *Phys. Med. Biol.*, vol. 58, no. 14, pp. 5007–5008, jul 2013.

[26] G. Alexandrakis, F. R. Rannou, and A. F. Chatziioannou, "Tomographic bioluminescence imaging by use of a combined optical-PET (OPET) system: a computer simulation feasibility study." *Phys. Med. Biol.*, vol. 50, no. 17, pp. 4225–4241, 2005.

[27] T. Saratoon, T. Tarvainen, S. R. Arridge, and B. T. Cox, "3D quantitative photoacoustic tomography using the δ-Eddington approximation," in

Proc. of SPIE, A. A. Oraevsky and L. V. Wang, Eds., vol. 8581, 2013, pp. 85 810V–1 − 85 810V–12.

[28] S. R. Arridge, M. Schweiger, M. Hiraoka, and D. T. Delpy, "A finite element approach for modeling photon transport in tissue." *Med. Phys.*, vol. 20, no. 2 Pt 1, pp. 299–309, 1993.

[29] F. M. Brochu, J. Joseph, M. Tomaszewski, and S. E. Bohndiek, "Light fluence correction for quantitative determination of tissue absorption coefficient using multi-spectral optoacoustic tomography," in *Proc. of SPIE*, V. Ntziachristos and R. Zemp, Eds., vol. 9539, 2015, pp. 95 390Z–1 − 95 390Z–8.

[30] H. J. van Staveren, C. J. Moes, J. van Marie, S. a. Prahl, and M. J. van Gemert, "Light scattering in Intralipid-10% in the wavelength range of 400-1100 nm." *App. Opt.*, vol. 30, no. 31, pp. 4507–4514, 1991.

[31] A. Dima, N. C. Burton, and V. Ntziachristos, "Multispectral optoacoustic tomography at 64, 128, and 256 channels." *J. Biomed. Opt.*, vol. 19, no. 3, p. 36021, 2014.

[32] R. Cubeddu, A. Pifferi, P. Taroni, A. Torricelli, and G. Valentini, "A solid tissue phantom for photon migration studies," *Phys. Med. Biol.*, vol. 42, pp. 1971–1979, 1997.

[33] S. Prahl, "Tabulated Molar Extinction Coefficient for Hemoglobin in Water." [Online]. Available: http://omlc.ogi.edu/spectra/hemoglobin/summary.html

[34] D. Yao, C. Zhang, K. Maslov, and L. V. Wang, "Photoacoustic measurement of the Grueneisen parameter of tissue," *J. Biomed. Opt.*, vol. 19, no. 1, p. 017007, 2014.